



Dodecahedral ZnO/C framework on reduced graphene oxide sheets for high-performance Li-ion battery anodes



Edmund Samuel ^{a,1}, Chanwoo Park ^{a,1}, Taegun Kim ^a, Bhavana Joshi ^b, Ali Aldalbahi ^c, Hamdah S. Alanzi ^c, Mark T. Swihart ^d, Woo Young Yoon ^{e,*}, Sam S. Yoon ^{a,**}

^a School of Mechanical Engineering, Korea University, Seoul, 136-713, Republic of Korea

^b Department of Physics, NES Science College, Swami Ramanand Teerth Marathwada University, Latur Road, Nanded, Maharashtra, 431606, India

^c Department of Chemistry, College of Science, King Saud University, Riyadh, 11451, Saudi Arabia

^d Department of Chemical & Biological Engineering and RENEW Institute, University at Buffalo, The State University of New York, Buffalo, NY, 14260-4200, USA

^e Department of Materials Science & Engineering, Korea University, Seoul, 02841, Republic of Korea

ARTICLE INFO

Article history:

Received 19 November 2019

Received in revised form

11 March 2020

Accepted 14 April 2020

Available online 18 April 2020

Keywords:

ZIF8

Rhombic dodecahedron

Lithium-ion battery

Anode

ABSTRACT

To prepare high-performance ZnO/C nanocomposite anode materials, dodecahedral ZIF-8 was first deposited on exfoliated reduced graphene oxide (rGO) by precipitation from methanol. The ZIF-8 was carbonized by annealing in argon to produce ZnO/C that retained the structure of the ZIF-8 template. ZIF-8-derived ZnO/C and ZnO/C/rGO were deposited over Cu substrates using low-cost, scalable supersonic cold spraying to facilitate the rapid production of Li-ion battery anodes. The synergy of the ZIF-8-derived dodecahedral nano-ZnO/C framework with rGO significantly enhanced conductivity, reduced aggregation, and shortened Li-ion transfer pathways. Electrochemical impedance spectroscopy showed enhanced Li-ion diffusion. The rGO/ZnO/C framework demonstrated a specific capacity of $1325 \text{ mAh} \cdot \text{g}^{-1}$ at a specific current of $100 \text{ mA} \cdot \text{g}^{-1}$. At a higher current of $2.5 \text{ A} \cdot \text{g}^{-1}$, the anode delivered a capacity of $525 \text{ mAh} \cdot \text{g}^{-1}$. The composite also showed a highly stable reversible capacity of $1063 \text{ mAh} \cdot \text{g}^{-1}$ after 300 cycles. The outstanding electrochemical performance of the rGO/ZnO/C sample was facilitated by the three-dimensional morphology of the exfoliated rGO and ZIF-8-derived dodecahedral porous ZnO/C structure. A quantitative comparison of specific capacity and capacity retention shows that the electrochemical performance of these rGO/ZnO/C composites exceeds that of previously-reported anodes based on ZnO, carbon, and/or rGO.

© 2020 Elsevier B.V. All rights reserved.

1. Introduction

Li is both the lightest and the smallest metallic element, making it uniquely well-suited for use in lightweight electrochemical devices [1]. In particular, Li-ion-based rechargeable batteries gain many of their advantages from these features. Portable devices such as smartphones, laptops, and cordless tools and appliances, as well as electric vehicles, utilize lightweight, high-energy-density, and high-specific-capacity Li-ion batteries (LIB) [2–5]. However, Li-ion batteries with even higher charge and discharge rates and energy storage capacities are desired to improve performance of these devices and

vehicles [5,6]. Nearly all current Li-ion batteries employ graphite, with a theoretical lithium uptake capacity of $372 \text{ mAh} \cdot \text{g}^{-1}$, as their anode material [7,8]. Replacing graphite with a material that exhibits higher lithium uptake capacity would increase overall energy storage capacity per mass or volume of battery. Researchers have investigated numerous metal oxides such as SnO_2 , Fe_2O_3 , SiO_2 , TiO_2 , Co_3O_4 , ZnO , and Mn_3O_4 for use as anode materials in Li-ion batteries [9–18]. ZnO [14], SnO_2 [19] and SiO_2 [13] have high theoretical lithium uptake capacities of 978, 1484, and $1965 \text{ mAh} \cdot \text{g}^{-1}$, respectively. Among these, ZnO undergoes a volume expansions of ~163% at its full capacity, while SnO_2 and SiO_2 expand by more than 300% during Li-ion insertion [17,20]. The dramatic volume changes of SnO_2 and SiO_2 degrade their performance as anode materials during long-term cycling [21]. In contrast, TiO_2 has minimal volume change (<4%) but also has a low theoretical capacity of $336 \text{ mAh} \cdot \text{g}^{-1}$ [11].

Preparation of nanocomposites with carbon is one way to mitigate the volume change that leads to degradation of SnO_2 and

* Corresponding author.

** Corresponding author.

E-mail addresses: wyyoon@korea.ac.kr (W.Y. Yoon), skyyoon@korea.ac.kr (S.S. Yoon).

¹ These authors have contributed equally.

ZnO during lithiation [19,22–25]. Such composite structures may also offer higher electronic and Li-ion conductivity. Metal oxide composites can use various forms of carbon including graphene, carbon nanotubes, or core–shell structures with carbon encasing the metal oxide. The carbon component can form electrically conductive networks that enhance the electrochemical performances of the active material. However, these composite electrode materials often fall far short of their theoretical lithium storage capacities; they may also fail to attain long-term metal oxide stability at higher current rates (as seen for Si and SiO₂ [26]). Producing nanocomposites with carbon by methods such as flexible core–shell electrode fabrication improves the stability, but simultaneously lowers the capacity of the overall active material. Nanocomposite structures with three-dimensional nanocarbon frameworks can enhance the capacity and the rate capability of Li-ion batteries, as they shorten the Li-ion diffusion pathways and thus increase the charge transport rate [27,28]. Creating such structures with a high metal oxide content and high surface area carbon will optimize performance.

Three-dimensional metal oxide/carbon frameworks can be derived from metal-organic frameworks (MOFs) [29]. The porous morphologies of MOFs consist of metal ion nodes connected by organic ligands. MOFs have attracted considerable recent attention across numerous fields where their tunable pore sizes, high crystallinity, and enormous variety of structures obtainable with different organic linkers are advantageous [28,30,31]. Numerous types of zeolitic organic framework materials have been reported [32–34]. One emerging subclass of MOFs is the set of dodecahedral frameworks formed by the bridging of Zn²⁺ with imidazolate (Im) linkers. The most well-studied of the Zn-based zeolitic imidazolate framework (ZIF) materials is perhaps ZIF-8 [35]. ZIF-8 replicates zeolitic structure by forming Zn–Im–Zn bonds with a 145° bond angle similar to that of Si–O–Si in aluminosilicate zeolites. ZIF-8 comprises zinc-ions and 2-methylimidazole organic linkers connected by these zeolite-like coordination bonds to create a crystalline porous microstructure. ZIF-8 crystals often adopt a dodecahedral morphology that reflects their underlying crystal structure. Like other MOFs, these ZIF-8 particles possess nanocavities and open channels through which Li-ions can be inserted and extracted. This property of ZIF-8 enables storage of a large amount of Li-ions and thus high energy storage capacity. In addition, the porous nature of ZIF-8 provides a buffer for volume expansion and contraction during the insertion and extraction of Li-ions. This ZIF can be pyrolyzed to produce a porous metal-oxide-loaded carbon that maintains much of the pore structure and high surface area of ZIF-8. The uniform distribution of zinc in porous carbon yields good conductivity and energy storage capacity [36,37]. Thus, good high-current-rate performance is expected from ZIF-8-derived anode materials.

In our group, electrospinning has been previously used to produce ZIF-8 nanofibers for application in LIBs [3,6]. A rhombohedral Ni@ZnO bimetallic oxide hosted on carbon nanofibers (CNF) was demonstrated as an anode material [3]. The carbon nanofibers were decorated with particles that retained the rhombic dodecahedral morphology of ZIF-8 [6]. While electrospinning is useful in producing various types of nanofibers for LIB applications, the method has not yet been optimized for large-scale production, as compared to supersonic cold spraying, which is rapid, non-vacuum, and scalable [38–40]. Any wet precursor can be atomized into the supersonic gas stream, which facilitates evaporation of the precursor such that only the non-volatile residues or suspended particles are deposited on a substrate. This promotes strong adhesion between deposited materials and the substrate. A recent review on supersonic cold spraying for energy storage applications is available in Ref. [38].

In this work, we report the cold-spray (CS) deposition of ZIF-8-derived carbon/ZnO and composites containing it on Cu substrates. CS is facile and easily scalable to industrial production levels, without requiring vacuum equipment. We show that the addition of reduced graphene oxide (rGO) to the ZIF-8-derived carbon/ZnO increased the stability and current-rate capability of the anode material. The presence of polyacrylonitrile enhanced the adhesion of rGO to the active material, facilitating Li-ion and electron transfer. We compared the superior performance of the prepared Li-ion battery anode reported here with those described in prior reports using ZIF-8-derived materials.

2. Experimental procedure

2.1. Materials

Polyacrylonitrile (PAN, $M_w = 150$ kDa) as a dispersant, *N,N*-dimethylformamide (DMF, 99.8%) as a solvent, zinc acetate dihydrate (ZnAc, Zn(CH₃COO)₂·2H₂O, ~98%), and 2-methylimidazole (2MI, ~99%) as reagents for ZIF-8 synthesis were purchased from Sigma-Aldrich. These chemicals, as well as rGO (N002-PDR, Angstrom Materials) and ZnO (100 nm, Sigma-Aldrich) were used as received without further purification. Methanol from Duksan Chemicals was employed as a solvent for ZIF-8 synthesis.

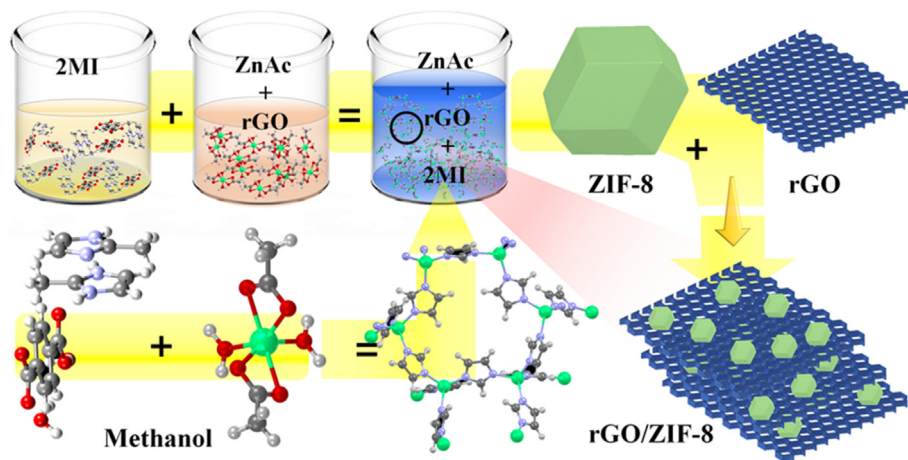
2.2. Chemical synthesis of ZIF-8 and rGO/ZIF-8

Hydrothermal processing has most often been used for ZIF-8 synthesis [41–44], but we used a simpler and faster precipitation route. The ZIF-8 particles were obtained from a 50-mL methanol solution containing a reagent mixture of 0.5 mmol ZnAc and 2 mmol 2MI. Visible ZIF-8 crystal formation began after about 10 min of mixing, as confirmed by a change in the solution appearance from transparent to turbid white (Supporting Information Fig. S1). ZnAc provided Zn²⁺ ions while 2MI provided imidazolium ions in methanol. These Zn²⁺ and imidazolium ions self-assemble to form the characteristic ZIF-8 rhombic dodecahedral morphology [3,6,45].

For the synthesis of rGO/ZIF-8 composite particles, 0.5 mmol ZnAc was dissolved in 50 mL methanol, to which 0.005 g rGO was added and ultrasonicated to disperse the rGO as exfoliated sheets. Then, 2 mmol 2MI was added and stirred, inducing ZIF-8 growth on the exfoliated rGO sheets. The process of selecting this quantity of rGO for use in the composite is discussed in supporting information along with SEM images showing the change in rGO/ZIF-8 nanocomposite morphology produced with different rGO loadings (Fig. S2). While further optimization of rGO content may be possible, the loading used here provides a reasonable starting point at which both rGO and ZIF-8-derived ZnO/C surfaces are accessible to the electrolyte in the nanocomposite. Scheme 1 illustrates the rGO/ZIF-8 composite particle synthesis. Finally, the ZIF-8 and rGO/ZIF-8 particles were centrifuged, washed, and dried for 24 h at 80 °C.

2.3. Deposition of ZIF-8 and rGO/ZIF-8

Dispersions of ZIF-8 (0.13 g) and rGO/ZIF-8 (0.13 g) were prepared separately using 40 mL DMF as a solvent; to each of these, 0.3 mL PAN (8 wt%)/DMF solution was added as a dispersant. Through a similar approach, we created a solution of pristine ZnO particles (100 nm, Sigma-Aldrich) for comparison to the ZIF-8-derived ZnO/C frameworks. Each dispersion was loaded in a syringe and pumped into a supersonic air stream, as is typical in the CS technique. The CS coating system, as presented in Fig. 1, comprises a supersonic nozzle, *x*–*z* stage, atomizer, and syringe pump,



Scheme 1. ZnAc reacts with rGO/2MI in the presence of methanol to form rGO/ZIF-8 composite particles.

along with an air tank and inline heater. The details of the CS system and the working procedure are discussed thoroughly in our earlier paper [46]. Table 1 lists the operating conditions maintained during deposition. The CS samples were further annealed in Ar at 700 °C for 60 min. Use of an annealing temperature higher than 700 °C causes losses of carbon content, as reported by He et al. [47] and Sun et al. [48]. Hence, we set the maximum annealing temperature at 700 °C. After annealing, the samples obtained from the single-component powders were named rGO and ZnO; those from the ZIF-8 dispersions were named ZnO/C and rGO/ZnO/C.

2.4. Physicochemical characterization

The phases of the composites were identified by X-ray diffraction (XRD; SmartLab, Rigaku). A Raman spectrometer (NRS-3100, Jasco) was used to analyze the graphitic and disordered C contents of the composites. The dodecahedral morphologies of the rGO/ZIF-8-derived composites were observed using a field-emission scanning

Table 1
Operating conditions of supersonic CS.

Spraying parameter	Values
Pressure (P_0) [bar]	2
Heater temperature [°C]	250
Flowrate [ml/min]	1.5
Traverse speed [mm/s]	35
Spraying distance [mm]	200
Number of passes	10

electron microscope (FESEM; S-5000, Hitachi, Ltd.) and a transmission electron microscope (TEM; JEM 2100F, JEOL Inc.). The TEM samples were prepared by CS of the composites directly onto Cu grids followed by annealing. Energy-dispersive X-ray (EDX) spectrometers configured within the SEM and TEM were used for elemental analysis. High angle annular dark field scanning transmission electron microscopy (HAADF STEM) was used for elemental

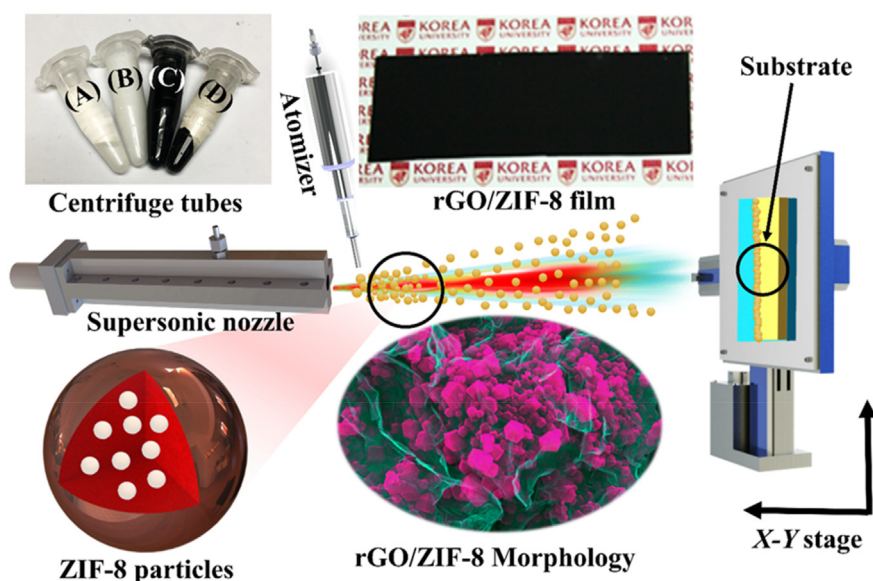


Fig. 1. Centrifuge tubes (A, D) containing separated ZIF-8 and rGO/ZIF-8 particles, and (B, C) dispersed ZIF-8 and rGO/ZIF-8 particles. Supersonic cold spray (CS) setup for deposition of ZIF-8 and rGO/ZIF-8 films on Cu; photograph of black-colored rGO/ZIF-8 film, and color rGO/ZIF-8 microstructure morphology processed using ImageJ software to highlight ZIF-8 (magenta) and rGO (cyan) characteristic structural features. (For interpretation of the references to color in this figure legend, the reader is referred to the Web version of this article.)

mapping. The elemental compositions and chemical states were determined by X-ray photoelectron spectroscopy (XPS; Theta Probe Base System, Thermo Fisher Scientific Co.). Thermogravimetric analysis (TGA) of mats was conducted using a TA Instruments Model SDT Q600 from 25 °C to 700 °C at a heating rate of 10 °C/min in air. For Brunauer-Emmett-Teller (BET) surface area measurements and analysis of pore volume, nitrogen adsorption and desorption isotherms of rGO/ZnO/C powder samples were measured with a volumetric adsorption apparatus (Tristar 3000, Micromeritics).

2.5. Electrochemical characterization

The various films on Cu foil were punched into 1.54-cm² circular sheets with an areal density of 0.9 mg/cm². The punched electrodes were used as working electrodes with 16-mm-diameter Li foils as the counter electrodes in CR2032-type coin cells. The electrodes were isolated from each other using Celgard 2400 polymer membranes (Celgard, Chungbuk, South Korea) as separators. The electrolyte used in the coin cells was a solution of 1-M LiPF₆ dissolved in ethylene carbonate, dimethyl carbonate, and ethyl methyl carbonate (1:1:1 by volume) (PuriEL, Soulbrain, Seongnam, South Korea). Galvanostatic charge–discharge tests of the coin cells were performed in the voltage range 0.05–3 V at 25 °C using a WBCS3000 battery cycler system (WonATech, Seoul, South Korea) for longer cycles at 0.1 C (where 1 C = 1000 mA·g⁻¹). Half-cells were subjected to current rate tests at 0.1, 0.2, 0.5, 1, 1.5, 2 and 2.5 C. Electrochemical impedance spectroscopy (EIS, VersaSTAT-3, Princeton Applied Research, USA) was performed over the frequency range 100 kHz–0.01 Hz with a perturbation voltage of 10 mV to analyze the resistance components and charge transfer kinetics [49].

3. Results and discussion

3.1. Materials properties

Fig. 2 shows SEM images of the rGO, ZnO, ZnO/C, and rGO/ZnO/C films at different magnifications. Cu substrates were used as current collectors for CS deposition of all samples. The rGO nanosheets are well dispersed and distributed homogeneously over the substrate. The SEM images of the rGO samples indicate their exfoliation (see Fig. 2a–c) via high-speed impact with the substrate. Fig. 2d–f shows ZnO nanoparticles and nanorods deposited over the Cu foil without much agglomeration. However, the particle size increased somewhat after annealing. The ZIF-8 particles after annealing in Ar atmosphere retain their rhombic dodecahedral structure, as seen in Fig. 2g–i. The shape of ZIF-8 is consistent with products of methanol-based synthesis in the literature [50,51]. The ZIF-8 particles decorated on exfoliated rGO sheets show lower degrees of ZIF-8 particle fusion even after annealing. The exfoliated rGO sheets provide space for the volume expansion of the ZIF-8-derived ZnO/C framework during lithiation. In addition, the average grain diameter of the ZnO/C framework decreased upon addition of rGO sheets. Moreover, as shown in Fig. 2j–l, the rGO/ZnO/C composites exhibit more uniform dodecahedral structure owing to the presence of rGO. Without the rGO shield, the dodecahedral structure is distorted during annealing, as seen in Fig. 2g–i, producing a different morphology from that of the rGO/ZnO/C composites. Figs. S3a and b compare the morphology of the rGO/ZnO/C samples before and after annealing. In Figs. S3c and d, the particle size change due to annealing is presented, showing a slight reduction (approximately 20 nm) in size after annealing. Elemental mapping of the rGO/ZnO/C framework is presented in Fig. S4. The rGO/ZnO/C nanocomposite shows uniform dispersion of ZnO/C derived from ZIF-8 over rGO.

Fig. 3 displays TEM images used to analyze the morphology and

microstructure of rGO/ZnO/C. The bright and contrasting curtain-like structures in Fig. 3a are the rGO sheets. The higher-magnification TEM image (Fig. 3b) clearly shows truncated dodecahedron structures that retain the framework structure of ZIF-8 and are highly porous. The selected-area electron diffraction (SAED) pattern in the inset of Fig. 3b shows a ring corresponding to the (101) plane of carbon (JCPDS 75-1621) arising from the rGO. The HAADF image in Fig. 3c and corresponding elemental mapping images in Fig. 3d–g shows that C, Zn, N and O are uniformly distributed within the ZIF-8-derived particles covering the rGO sheets. The EDS spectrum in Fig. 3h also confirms the presence of these elements in the rGO/ZnO/C films. The porous nature of rGO, ZnO, ZIF-8 derived ZnO/C, and rGO/ZnO/C was quantified by N₂ adsorption-desorption measurements presented in supporting information, Fig. S6. The measured surface areas of rGO, rGO/ZnO/C and ZnO/C were 2212, 1283, and 1782 m²/g respectively. The surface area of the purchased ZnO starting material was only 14.6 m²/g.

Wide-angle powder XRD of the as-synthesized ZIF-8 is shown in Fig. S5. The peaks of various planes appearing in the pattern match those of simulated ZIF-8 XRD patterns, confirming the formation of ZIF-8 [52–54]. The diffraction patterns of the carbonized samples of rGO, ZnO (powder from Sigma Aldrich), ZIF-8-derived ZnO/C, and rGO/ZnO/C were collected at room temperature by 0.01°-step scanning in the range of 10–80°. The characteristic graphene peaks observed at 26° and 43.5° in the XRD patterns of the rGO and rGO/ZnO/C samples in Fig. 4a and indicated by ♦ symbols correspond to the (002) and (101) planes of rGO nanosheets (JCPDS card no. 75-1621). The CS-deposited ZnO film from ZnO powder shows peaks at 31.85, 34.51, 36.29, 47.62, 56.69, 62.87, 66.50, 68.03, and 69.12°, corresponding to the (100), (002), (101), (102), (110), (103), (200), (112), and (201) planes, respectively, of the hexagonal wurtzite ZnO structure (JCPDS card no. 36-1451) [55,56].

The carbonized ZIF-8-derived ZnO/C pattern shows a broad peak near 21°, corresponding to the carbon from the organic framework after annealing. ZIF-8 particles were dried in atmospheric air at a temperature of 80 °C for 24 h. The ZIF-8 particles were not prone to oxidation at this relatively low temperature of 80 °C. This oxygen scarcity in ZIF-8 continued when they were annealed at 700 °C in an inert environment with argon. Under these conditions, ZIF-8 decomposes to produce amorphous ZnO and thus no characteristic peaks of ZnO were observed. Bai et al. [57] reported that at a carbonization temperature lower than the melting point of Zn (907 °C) ZIF-8 decomposes to form crystalline ZnO which is confined by the porous carbon framework. However, in this case, the presence of carbon (from rGO) may retard the crystallization of ZnO [19].

Raman spectroscopy was employed to differentiate defective (D) and graphitic (G) carbon derived from the organic framework and rGO. The Raman spectra in Fig. 4b show peaks at ~1360 cm⁻¹, corresponding to the D bands of the samples. The peaks attributed to the G bands are observed near 1590 cm⁻¹, assigned to the E_{2g} mode [58,59]. The D-to G-peak intensity ratios I_D/I_G for rGO, ZnO, ZnO/C, and rGO/ZnO/C are approximately 1.15, 1.18, 1.32, and 1.49, respectively. I_D/I_G is nonzero in ZnO because of the C derived from PAN used in the deposition solution as a dispersant. The ZIF-8-derived ZnO/C and rGO/ZnO/C show higher I_D/I_G values, suggesting that C from the organic framework is generally defective, hindering the development of graphitic phase (or rGO in the rGO/ZnO/C case). Further, higher I_D/I_G values indicate more defects in the films, which are beneficial because they improve Li-ion diffusion and provide more intercalation sites for Li-ion storage [60–62].

The overall XPS spectrum and high resolution XPS scans revealing the chemical state of elements in the ZIF-8-derived rGO/ZnO/C composite are presented in Fig. S7. The survey spectrum in Fig. S7a indicates the presence of carbon, zinc, nitrogen and oxygen

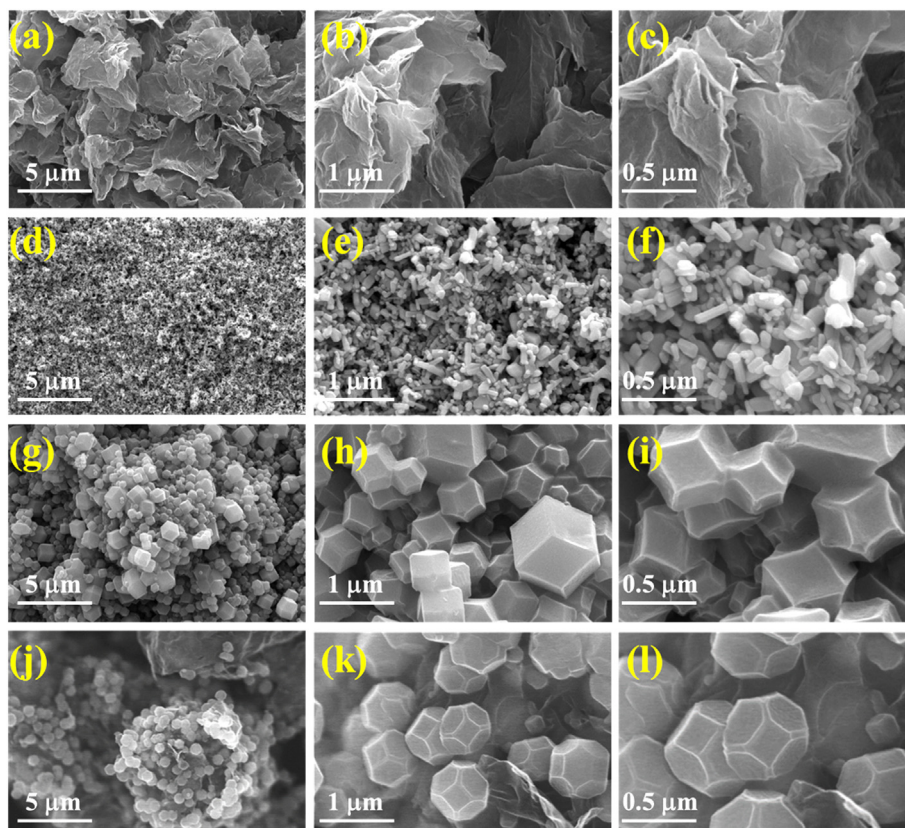


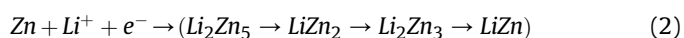
Fig. 2. SEM images of (a–c) rGO film, (d–f) ZnO film, (g–i) ZnO/C composite film, and (j–l) rGO/ZnO/C composite film.

together in the composite sample, consistent with the elemental mapping shown in Fig. S4. The Zn 2p core spectrum (Fig. S7b) shows two peaks at 1021.9 and 1044.9 eV for Zn 2p_{3/2} and Zn 2p_{1/2} with a spin orbit binding energy difference of 23 eV indicating formation of ZnO with Zn present as Zn²⁺ [63]. The metal oxide peaks are also evident from the O 1s spectrum. The O 1s spectrum in the inset of Fig. S7b exhibits three peaks at 530, 532 and 533.5 eV [64]. The presence of a peak at lower binding energy, i.e., at 530 eV in Fig. S7b inset, is attributed to O²⁻ ions. Thus, the peak at 530 eV demonstrating the presence of O²⁻, combined with the Zn 2p peaks (1021.9 and 1044.9 eV) indicating the Zn²⁺ oxidation state indicate the presence of Zn–O bonding. Further, the peaks at binding energies of 532 and 533.5 eV are attributed to Zn–O–H and O–H. The C 1s core spectrum in Fig. S7c shows three peaks at 284, 286 and 287 eV attributed to C=C sp², C–C sp³ and C=O, respectively. The presence of rGO is evident from the C=C sp² peak. The high resolution N 1s spectrum (Fig. S7d) shows peaks at 398, 399 and 401 eV corresponding to pyridinic, pyrolic and graphitic nitrogen. The dominance of the pyrolic band is consistent with nitrogen incorporation from the imidazole of ZIF-8.

3.2. Electrochemical performance

Fig. 5a and b shows the discharge–charge profiles of the cells containing ZnO/C and rGO/ZnO/C samples, respectively, at a current of 100 mA·g⁻¹ and voltages of 0.05–3 V (vs. Li/Li⁺). The ZnO/C sample shows an initially sharp voltage discharge to 0.8 V (*N* = 1) and then forms a plateau region at ~0.5 V. The plateau may arise from electrochemical reactions between ZnO and Li-ions that cause the oxidation of Li ions and reduction of ZnO, as shown in Eq. (1). The reduced metallic Zn can form an alloy with Li-ions. Thus, the

metallic Zn participates in a multistep alloying reaction with Li, as demonstrated by Eq. (2). However, the lack of any clear plateau in the subsequent charge cycle indicates a change in the active material's microstructure.



For rGO/ZnO/C (Fig. 5b) the discharge–charge profile looks somewhat different because of the presence of rGO and possibly from the faster charge transfer and shorter pathway for Li-ion storage. Additionally, the presence of rGO sheets provides Li ions with adsorption and intercalation sites, in addition to those in the dodecahedral ZnO/C framework decorated over the rGO sheets. The discharge profile clearly shows the superior performance of rGO/ZnO/C compared to that of the ZnO/C sample. The ZnO/C (derived from ZIF-8) sample shows 65% retention after *N* = 200 cycles, while the rGO/ZnO/C sample demonstrates a much higher retention of ~80% after the same number of cycles. The differential capacities (Fig. 5c and d) of both samples show three peaks. The peaks at 0.18 V (ZnO/C) and 0.2 V (rGO/ZnO/C) indicate alloying of Zn and Li. The sharp peak at 0.52 V for the ZnO/C sample possibly indicates the formation of a thicker solid electrolyte interface (SEI) layer during alloying of Li and Zn. However, the broad and low-intensity peak appearing at 0.51 V for the rGO/ZnO/C sample is due to the presence of rGO that restricted Li₂O formation. The rGO provides a shorter pathway for Li-ion diffusion and hence the possibility of a thin SEI layer arises. The SEI layer formation is completed during the first cycle (*N* = 1) because the electrochemical reaction includes both reversible and irreversible capacity generation. An additional peak at 0.85 V appears for rGO/ZnO/C, corresponding to the

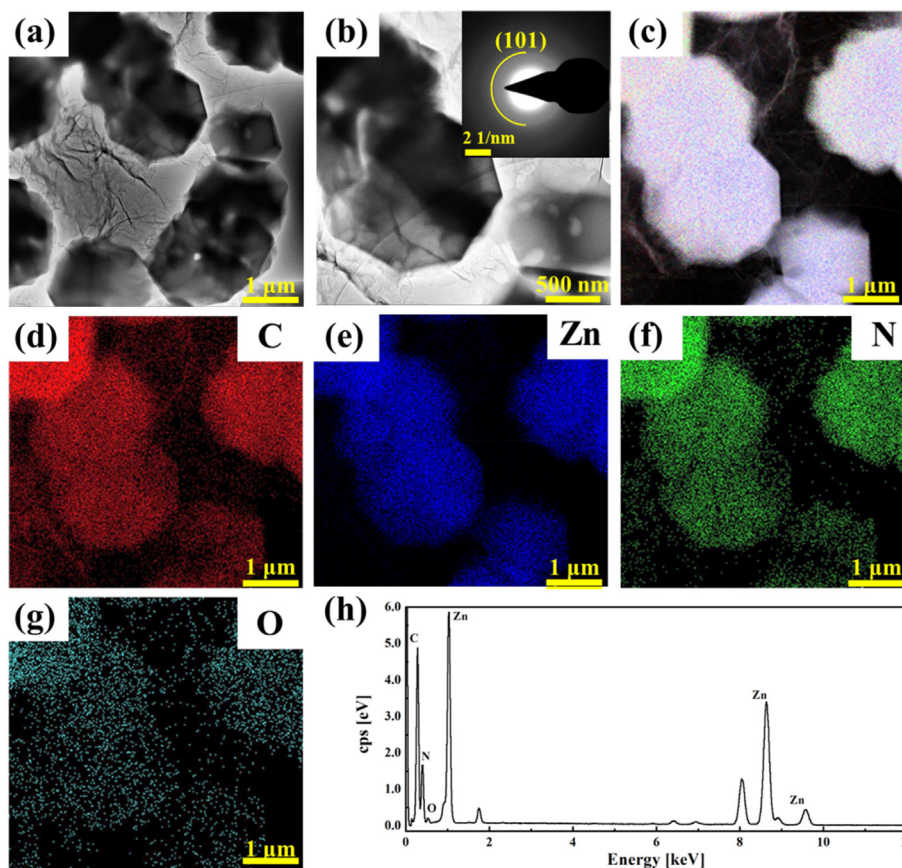


Fig. 3. (a) TEM image of rGO/ZnO/C, (b) higher magnification image with SAED pattern shown as an inset, (c) HAADF TEM, (d–g) Elemental mapping images of C, Zn, N and O. (h) EDS spectrum of rGO/ZnO/C sample.

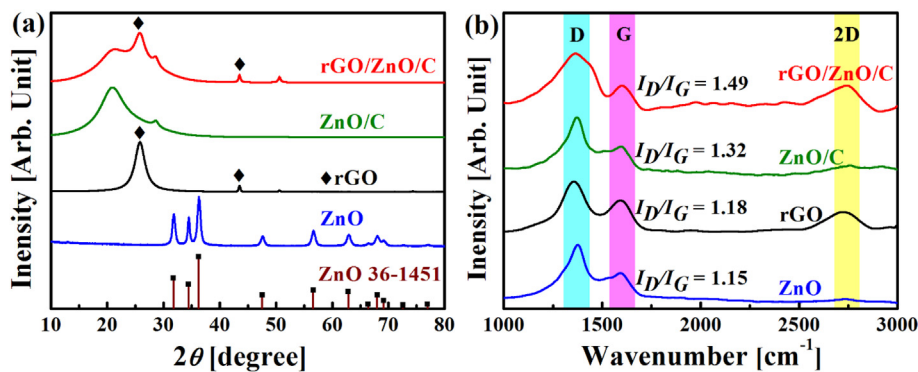


Fig. 4. (a) XRD patterns and (b) Raman spectra of various samples as labelled.

reduction of ZnO to metallic Zn by the insertion of Li-ions [49]. Thus, we infer that Li-ion insertion into rGO/ZnO/C begins much earlier compared to insertion into the ZnO/C sample due to bridging of ZIF-8-derived ZnO–N along with buffering of LiZn, ZnO, and Li₂O during the lithiation/de-lithiation process. As a result the first capacity of rGO/ZnO/C (1325 mAh·g⁻¹, in spite of thin SEI i.e. lower electrolyte decomposition) is higher than ZnO/C (1273 mAh·g⁻¹). Further, similar to the differential capacity plot (in Fig. 5d), the CV curve of the rGO/ZnO/C sample for N = 1 in Fig. S8 shows peaks at 0.91, 0.77 and 0.46 V in the cathodic scan (i.e. Li insertion) due to reduction of ZnO to Zn along with Li₂O formation, followed by alloying of Zn with Li. The peak for ZnO reduction

appeared at 0.9 V because of improved reaction kinetics owing to the presence of rGO. The anodic scan (Li extraction) shows broad peaks related to de-alloying and re-oxidation of Zn at 0.5 and 1.1V respectively.

Current rate variation during the electrochemical capacity measurement is critical to understand the Li-ion diffusion and energy storage characteristics of the samples. At a lower current rate (100 mA·g⁻¹), the specific capacity of the ZnO sample during the first discharge cycle was observed to be the highest (1352 mAh·g⁻¹, see Fig. S9) among all the samples. The higher capacity could arise from the well-known phenomenon of thicker SEI layer formation. However, the ZnO sample did not perform well at increased current

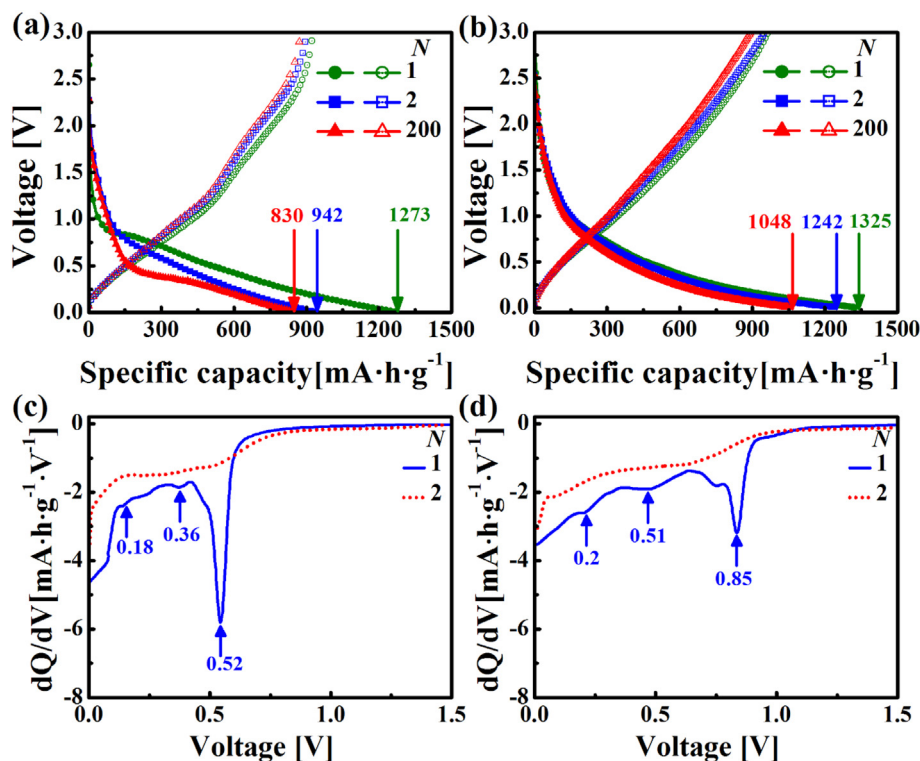


Fig. 5. Discharge–charge profiles of (a) ZnO/C and (b) rGO/ZnO/C. Differential capacity plots of (c) ZnO/C and (d) rGO/ZnO/C for $N = 1$ and 2.

rates because of the continued expansion and contraction of the ZnO particles with lithium insertion and extraction. This cyclic volumetric change caused pulverization, which consistently decreased the capacity. Additionally, the drastic fall of the specific capacity and poor retention for the ZnO sample at increasing current rate confirmed the irreversible electrochemical reaction and the occurrence of pulverization. Further, as the current rate increased, the faster movement of the Li-ions limited their diffusion inside the active material, reducing the effective capacity. Overall, the material showed significant capacity fading as well as poor rate capability. On the other hand, although rGO has a low theoretical capacity of $372 \text{ mAh}\cdot\text{g}^{-1}$, the rGO-containing sample demonstrated good capacity and promising capacity retention (see Fig. S9).

The ZnO/C composite derived from ZIF-8 after annealing at 700°C in Ar delivered an initial reversible capacity of $1048 \text{ mAh}\cdot\text{g}^{-1}$ at a current rate of $100 \text{ mA}\cdot\text{g}^{-1}$. Each sample was tested at increasing current rates from 100 to $2500 \text{ mA}\cdot\text{g}^{-1}$. For each current rate, testing was performed for 10 charge–discharge cycles; after $N = 70$ cycles, the current rate was decreased in reverse order (Fig. 6a). Finally, the current rate of $100 \text{ mA}\cdot\text{g}^{-1}$ was maintained for 200 cycles. As the nanoparticles were mostly amorphous-where Zn is present at nodal sites of the C framework, the volume buffering is improved relative to that of the pristine ZnO sample (see Fig. 2), yielding good capacity retention after 200 cycles. Similarly, the rGO/ZnO/C also shows capacity recovery and superior performance compared to ZnO/C because of the faster charge transport enabled by rGO. The rGO content in the rGO/ZnO/C sample from Fig. 6a is 0.005 g (i.e. $\text{rGO}_{0.005}/\text{ZnO}/\text{C}$). The Coulombic efficiency (CE) in Fig. 6a was 55 and 60% for ZnO/C and rGO/ZnO/C respectively after the first cycle, increased to 95 and 96% after the second cycle and remained the same after 200 cycles. The effect of varying rGO content from 0.001 g to 0.008 g (i.e. $\text{rGO}_{0.001}/\text{ZnO}/\text{C}$ and $\text{rGO}_{0.008}/\text{ZnO}/\text{C}$) on the current rate capability is shown in Fig. S10; their current rate capability is poorer than that of the $\text{rGO}_{0.005}/\text{ZnO}/\text{C}$ sample from Fig. 6a. The limited performance of the

0.001 g case is explained by the reduced charge transfer kinetics with reduced rGO content. Conversely, when rGO is relatively excessive, as in the 0.008 g case, it facilitates a carbon-rich environment which in turn reduces the relative concentration of ZnO. Graphite stores Li-ions via intercalation and has a theoretical capacity of $372 \text{ mAh}\cdot\text{g}^{-1}$ while ZnO has a theoretical capacity of $978 \text{ mAh}\cdot\text{g}^{-1}$. Therefore, the reduced content of ZnO with respect to that of rGO would decrease the overall capacity. When rGO was decorated with ZnO/C, yielding a three-dimensional framework, the coulombic efficiency improved. The rGO/ZnO/C sample may have a much thinner SEI layer than the other samples. The thickness variation of the SEI layer can be hypothetically inferred based on the coulombic efficiency when $N = 1$ and the first reversible discharge capacity ($N = 2$) of each sample. The capacity retention graph as a function of current density, shown in Fig. 6b, clearly depicts 60% and 58% retention by the rGO/ZnO/C and ZnO/C samples, respectively, owing to the highly porous, interconnected, ordered framework obtained from the parent ZIF-8. The carbon content from ZIF-8 and rGO and the ZnO content from ZIF-8 were estimated from TGA analysis, as presented in supporting information Fig. S11. Combining the carbon and ZnO content with their corresponding theoretical capacities yields an expected capacity of $456 \text{ mAh}\cdot\text{g}^{-1}$, which is lower than the observed capacity. However, the presence of nitrogen, high porosity, and specific structure of carbon can enhance the capacity as obtained in LIB data.

Fig. 6c illustrates the long-term cycling performance of the samples within the voltage window $0.05\text{--}3.0 \text{ V}$ (vs. Li/Li^+) at a current of $100 \text{ mA}\cdot\text{g}^{-1}$. The poor electrochemical performance and lower coulombic efficiency of the sample deposited using ZnO particles are clear from Fig. 6. However, the rGO, ZnO/C, and rGO/ZnO/C anodes show excellent cyclability up to 300 cycles. The pristine rGO electrode demonstrates a capacity ~ 2.25 times lower ($\sim 141 \text{ mAh}\cdot\text{g}^{-1}$) than its theoretical capacity ($372 \text{ mAh}\cdot\text{g}^{-1}$). The retained discharge capacities after 300 cycles are $\sim 89, 391, 843$ and $1065 \text{ mAh}\cdot\text{g}^{-1}$ for rGO, ZnO, ZnO/C, and rGO/ZnO/C, respectively.

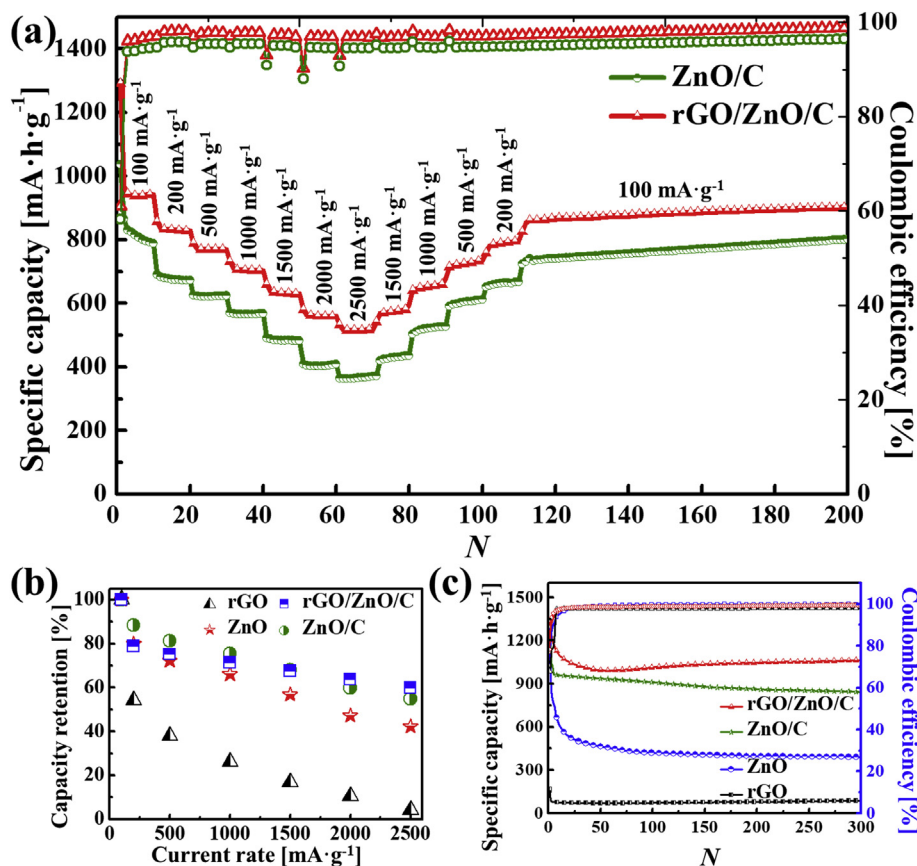


Fig. 6. (a) Electrochemical testing of ZnO/C and rGO/ZnO/C at variable current rate, (b) capacity retention as a function of current rate, and (c) long-term cycling capacity and coulombic efficiency of various samples at 100 mA·g⁻¹.

The corresponding capacity retentions for the respective cases are 53, 30, 64 and 80% after 300 cycles. In particular, the rGO/ZnO/C composite electrode shows excellent cyclic stability with ~80% capacity retention, which is attributed to the good adhesion and uniform decoration of ZnO/C on the exfoliated rGO sheets. The performance of rGO/ZnO/C under extended cycling is also demonstrated in Fig. S12 at a high current rate of 2500 mAh·g⁻¹. The coulombic efficiency after a few cycles approaches 100% and high capacity retention with respect to the first reversible capacity (78%) after 300 cycles confirms the excellent performance of rGO/ZnO/C. The high specific capacity retention value demonstrated by rGO/ZnO/C further supports the significance of the ZnO/C three-dimensional dodecahedra decorating the rGO. The synergy of the ZnO/C framework with rGO effectively accommodates the volume expansion/contraction during discharging and charging. The synergistic impact of rGO and ZnO/C leads to faster and shorter pathways for Li-ion transport and, as discussed earlier for the differential capacity measurements, accommodates more Li-ions and hence provides higher capacity than ZnO/C in spite of the larger ZnO concentration of ZnO/C. Moreover, the rGO in the rGO/ZnO/C nanocomposite suppresses particle aggregation upon repeated charge–discharge cycling as observed in the post-cycling SEM images shown in supporting information Fig. S13. Therefore, the rGO/ZnO/C sample delivers enhanced electrochemical reversibility and cycling efficiency compared with ZnO and the ZnO/C composite without rGO. In addition, rGO increases the conductivity of the active oxide materials. Hence, the rGO/ZnO/C sample exhibits improved rate capability and cycling stability. Finally, when compared with various morphologies of ZnO/C reported elsewhere,

our samples show better capacities, as summarized in Tables 2 and 3.

Fig. 7a shows the results of EIS analysis. The Nyquist plots are used to investigate the kinetics of the rGO, ZnO, ZnO/C, and rGO/ZnO/C samples with Li as a reference electrode. The Nyquist plots show the variation of imaginary impedance (Z'') as a function of real impedance (Z'), which indicates electron transport phenomena and Li-ion diffusion behaviors for each sample. The solution resistances (R_s) are 2, 8, 5, and 2.1 Ω for rGO, ZnO, ZnO/C, and rGO/ZnO/C, respectively. The solution resistance comprises the resistances of the current collectors, electrolyte, active material, and separator. All samples show semicircular arcs at high to medium frequencies. The semicircle diameters represent the charge-transfer resistances (R_{ct}) corresponding to the activation kinetics. The semicircle arc formation may be from the adsorption or redox reaction of Li ions with active electrochemical sites. The Li ions overcome the diffusion barrier at the medium-to low-frequency regime indicated by the inclined line, also known as the Warburg region. The impedance data were fit to the Randles equivalent circuit, shown in the inset of Fig. 7a. The curve fitting (dotted lines in Fig. 7a) yielded R_{ct} values of 92, 174, 102, and 99 Ω for rGO, ZnO, ZnO/C, and rGO/ZnO/C. The sample of only rGO shows the lowest R_s and R_{ct} , while that of ZnO has larger charge transfer resistance and slower Li-ion diffusion. However, ZnO derived from ZIF-8 shows improved conductivity because of its interconnected carbon network. The optimal rGO/ZnO/C composite sample demonstrates R_s and R_{ct} values that are only slightly higher than those of the rGO sample. Thus, the balance of charge transfer and energy storage sites is optimized for the rGO/ZnO/C case, as observed from Figs. 5

Table 2

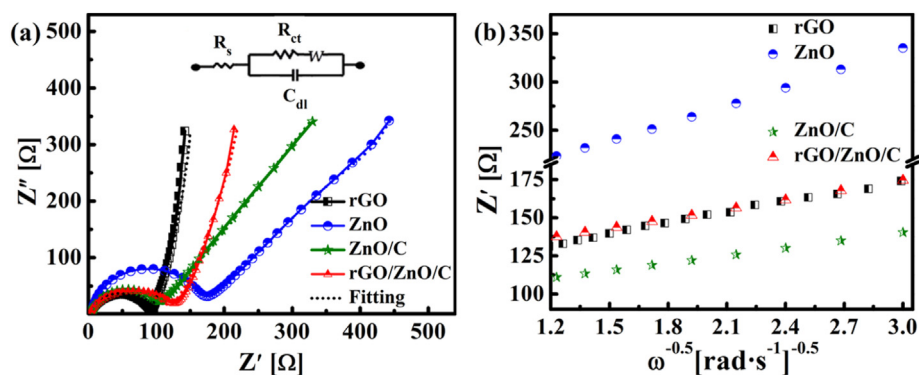
Comparison of reversible capacities of various ZnO/C composite-based Li-ion battery anodes with those in this work.

Materials	Morphology	Reversible capacity (mAh·g ⁻¹)	Current density (mA·g ⁻¹)	Ref.
ZnO@C	cubic	335	100	[22]
ZnO-C-rGO	nanofibers	472	500	[23]
ZnO/C	yolk-shell spheres	212	1000	[24]
ZnO/G	nanosheets	400	1000	[24]
ZnO/G	nanocomposites	400	1000	[25]
ZnO@C	peapod-like	414	1000	[14]
ZnO-G-10	nanosheets	415	1000	[15]
ZnO/NC-Z	nanorods	544	1000	[35]
ZnO@CF	nanospheres	288	2000	[16]
ZnO@C	peapod-like	331	2000	[14]
rGO/ZnO/C	dodecahedral	629	1500	Present
rGO/ZnO/C	dodecahedral	525	2500	Present

Table 3

Performance comparison of ZIF-8 derived anodes for LIBs with those in this work.

Materials	Capacity (mAh·g ⁻¹)	Current density (mA·g ⁻¹)	Cycles	Capacity retention (%)	Ref.
Organic-coated ZIF-8 nanocomposites	739	50	50	59	[29]
ZnO/ZnO@C	1442	100	50	58	[36]
ZnO/N-CF	1922	98	100	61	[37]
ZnO/NC-Z NRDs	1011	200	200	70	[35]
EEG-PC-ZnO	~1400	98	100	53	[49]
rGO/ZnO/C	1325	100	300	80	Present

**Fig. 7.** EIS analysis: (a) Nyquist plot (inset: equivalent circuit). (b) The relationship between Z' and the inverse square root of angular frequency in Warburg diffusion tail region.

and 6. Because all of the samples show different morphologies, the Li-ion diffusion varies, as indicated by the inclinations of impedance, in a manner corresponding to the changes in the R_{ct} values of the samples. To investigate the stability of the sample after cycling, EIS measurements were carried out as shown in Fig. S14. As expected rGO, ZnO/C and rGO/ZnO/C showed low R_{ct} values of 35, 77 and 71 Ω , respectively when fitted with Randles equivalent circuit. The lower charge transfer impedance for rGO, ZnO/C and rGO/ZnO/C samples suggests structural stability during long-term cycling. However, the ZnO sample displayed a higher R_{ct} value (227 Ω) after fitting, which may be due to thick SEI layer formation.

Fig. 7b shows the graph of real impedance as function of $\omega^{-0.5}$ in the low-frequency Warburg or Li-ion diffusion region. The Li-ion diffusion rates D can be extracted from the Warburg regions of the Nyquist plots using Eq. (3):

$$D = 0.5(RT / An^2F^2\sigma_w C)^2 \quad (3)$$

where D is the diffusion coefficient, R is the gas constant, T is the absolute temperature, A is the electrode area, n is the number of involved electrons, F is Faraday's constant, σ_w is the Warburg

coefficient, and C is the Li-ion concentration (mol/cm⁻³) in the solid. The inclined line of the Nyquist plot is related to the real impedance (Z') and σ_w as shown in Eq. (4):

$$Z' = R_s + R_{ct} + \sigma_w \omega^{-0.5} \quad (4)$$

By using Eqs. (3) and (4), we estimate diffusion coefficients of 5.0×10^{-8} , 5.6×10^{-9} , 1.9×10^{-8} , and 2.1×10^{-8} for rGO, ZnO, ZnO/C, and rGO/ZnO/C, respectively. The estimated diffusion coefficients suggest that Li-ion diffusion was faster for rGO/ZnO/C samples than for ZnO and ZnO/C. However, the exfoliated rGO showed even higher diffusion of Li-ions. The capacity delivered by rGO is lower than that of the composite because rGO stores Li ions only through adsorption, without other electrochemical reactions such as reduction or alloying. This indicates that ZIF-8-derived ZnO loading on rGO reduces the electron/Li-ion transfer pathways.

Fig. 8a illustrates the faster charge transfer in the two-dimensional rGO sheets, while Fig. 8b depicts Li-ion transfer within the three-dimensional ZIF-8-derived ZnO/C. The nano- and sub-micrometer particles of ZnO/C show fused and adjoining structures from the supersonic impact of the SC process, allowing rapid Li-ion transfer and higher currents, along with volume buffering by

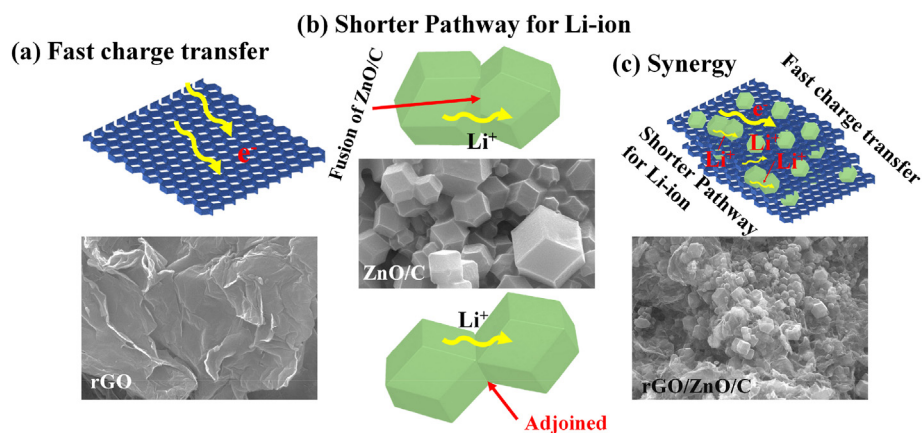


Fig. 8. Schematics of Li-ion transfer behaviors in (a) rGO, (b) ZnO/C, and (c) rGO/ZnO/C films.

the C framework. Despite the surface morphology and electrochemical stability of the ZnO/C particles, the lower conductivity hinders their potential. The third configuration of the rGO/ZnO/C composite film with rGO provides excellent structural morphology as shown in Fig. 8c, solving the issues of slow Li-ion and charge transfer during discharging and charging cycles. Thus, we conclude that the presence of rGO sheets enforces the adjoining connections between the ZnO/C and electrolyte by providing conductive passages, while the three-dimensional surface morphology of ZnO/C promotes volume buffering.

4. Conclusions

We demonstrated a facile approach for producing three-dimensional coordinated dodecahedral ZIF-8 and ZIF-8 decorated on rGO. Annealing ZIF-8 and ZIF-8 decorated on rGO at 700 °C produced ZnO/C and rGO/ZnO/C, respectively. The rGO/ZnO/C composite delivered significantly enhanced specific capacity compared to electrodes comprising ZnO particles, ZIF-8-derived ZnO/C, or rGO alone. The rGO/ZnO/C composite also exhibited 81% capacity retention and excellent cycling behavior. The remarkable performance of rGO/ZnO/C was explained by the inherent porosity and 3D dodecahedral morphology retained from the ZIF-8 precursor, which buffered volume expansion during lithium ion insertion, while rGO promoted faster charge transport. The non-vacuum cold-spray deposition process is rapid and scalable, demonstrating its potential for mass production of the proposed Li-ion electrodes.

Author contribution

Edmund Samuel Conceptualization, experiments and manuscript preparation. Chanwoo Park Data presentation, experiments and Sample fabrication. Taegun Kim Data presentation and Sample fabrication. Bhavana Joshi Data analysis and Manuscript preparation. Ali Aldalbahi Oversight and Validation. Hamdah S. Alanzi Validation. Mark T. Swihart Manuscript preparation. Woo Young Yoon Supervising the project, and manuscript preparation. Sam S. Yoon Supervising the project, and manuscript preparation.

Declaration of competing interest

The authors declare that they have no known competing financial interests or personal relationships that could have appeared to influence the work reported in this paper.

Acknowledgement

This research was supported by the Technology Development Program to Solve Climate Changes of the National Research Foundation (NRF) funded by the Ministry of Science, ICT & Future Planning (NRF- 2016M1A2A2936760) and NRF-2020R1A2C1012838. The authors acknowledge King Saud University, Riyadh, Saudi Arabia, for funding this work through Researchers Supporting Project number (RSP-2019/30).

Appendix A. Supplementary data

Supplementary data to this article can be found online at <https://doi.org/10.1016/j.jallcom.2020.155208>.

References

- [1] N. Nitta, F. Wu, J.T. Lee, G. Yushin, Li-ion battery materials: present and future, *Mater. Today* 18 (2015) 252–264.
- [2] M.-S. Balogun, H. Yang, Y. Luo, W. Qiu, Y. Huang, Z.-Q. Liu, Y. Tong, Achieving high gravimetric energy density for flexible lithium-ion batteries facilitated by core–double-shell electrodes, *Energy Environ. Sci.* 11 (2018) 1859–1869.
- [3] B. Joshi, E. Samuel, Y.I. Kim, M.-W. Kim, H.S. Jo, M.T. Swihart, W.Y. Yoon, S.S. Yoon, Hierarchically designed ZIF-8-derived Ni@ ZnO/carbon nanofiber freestanding composite for stable Li storage, *Chem. Eng. J.* 351 (2018) 127–134.
- [4] C. Zhang, S. Liu, Y. Qi, F. Cui, X. Yang, Conformal carbon coated TiO₂ aerogel as superior anode for lithium-ion batteries, *Chem. Eng. J.* 351 (2018) 825–831.
- [5] G. Zubi, R. Dufo-López, M. Carvalho, G. Pasaoglu, The lithium-ion battery: state of the art and future perspectives, *Renew. Sustain. Energy Rev.* 89 (2018) 292–308.
- [6] E. Samuel, B. Joshi, M.-W. Kim, Y.-I. Kim, S. Park, T.-G. Kim, M.T. Swihart, W.Y. Yoon, S.S. Yoon, Zeolitic imidazolate framework-8 derived zinc oxide/carbon nanofiber as freestanding electrodes for lithium storage in lithium-ion batteries, *J. Power Sources* 395 (2018) 349–357.
- [7] Y. Zhang, K. Hu, Y. Zhou, Y. Xia, N. Yu, G. Wu, Y. Zhu, Y. Wu, H. Huang, A facile, one-step synthesis of silicon/silicon carbide/carbon nanotube nanocomposite as a cycling-stable anode for lithium ion batteries, *Nanomaterials* 9 (2019) 1624.
- [8] Y. Zhang, J. Ren, T. Xu, A. Feng, K. Hu, N. Yu, Y. Xia, Y. Zhu, Z. Huang, G. Wu, Covalent bonding of Si nanoparticles on graphite nanosheets as anodes for lithium-ion batteries using diazonium chemistry, *Nanomaterials* 9 (2019) 1741.
- [9] W. Dong, J. Xu, C. Wang, Y. Lu, X. Liu, X. Wang, X. Yuan, Z. Wang, T. Lin, M. Sui, A robust and conductive black tin oxide nanostructure makes efficient lithium-ion batteries possible, *Adv. Mater.* 29 (2017) 1700136.
- [10] Z. Jin, M. Yang, S.-H. Chen, J.-H. Liu, Q.-X. Li, X.-J. Huang, Tin oxide crystals exposed by low-energy {110} facets for enhanced electrochemical heavy metal ions sensing: x-ray absorption fine structure experimental combined with density-functional theory evidence, *Anal. Chem.* 89 (2017) 2613–2621.
- [11] B. Joshi, E. Samuel, H.S. Jo, Y.-I. Kim, S. Park, M.T. Swihart, W.Y. Yoon, S.S. Yoon, Carbon nanofibers loaded with carbon nanotubes and iron oxide as flexible freestanding lithium-ion battery anodes, *Electrochim. Acta* 253 (2017) 479–488.
- [12] T. Jiang, F. Bu, X. Feng, I. Shakir, G. Hao, Y. Xu, Porous Fe₂O₃ nanoframeworks encapsulated within three-dimensional graphene as high-performance

- flexible anode for lithium-ion battery, *ACS Nano* 11 (2017) 5140–5147.
- [13] N. Yan, F. Wang, H. Zhong, Y. Li, Y. Wang, L. Hu, Q. Chen, Hollow porous SiO₂ nanocubes towards high-performance anodes for lithium-ion batteries, *Sci. Rep.* 3 (2013) 1568.
- [14] Y. Hao, S. Wang, J. Zeng, H. Li, P. Yang, B. Liu, S. Zhang, Y. Xing, A peapod-like ZnO@C design with internal void space to relieve its large-volume-change as lithium-ion battery anode, *Ceram. Int.* 44 (2018) 1321–1327.
- [15] M. Yu, A. Wang, Y. Wang, C. Li, G. Shi, An alumina stabilized ZnO–graphene anode for lithium ion batteries via atomic layer deposition, *Nanoscale* 6 (2014) 11419–11424.
- [16] C. Xiao, S. Zhang, S. Wang, Y. Xing, R. Lin, X. Wei, W. Wang, ZnO nanoparticles encapsulated in a 3D hierarchical carbon framework as anode for lithium ion battery, *Electrochim. Acta* 189 (2016) 245–251.
- [17] H. Wu, Y. Wang, C. Zheng, J. Zhu, G. Wu, X. Li, Multi-shelled NiO hollow spheres: easy hydrothermal synthesis and lithium storage performances, *J. Alloys Compd.* 685 (2016) 8–14.
- [18] G. Wu, Z. Jia, Y. Cheng, H. Zhang, X. Zhou, H. Wu, Easy synthesis of multi-shelled ZnO hollow spheres and their conversion into hedgehog-like ZnO hollow spheres with superior rate performance for lithium ion batteries, *Appl. Surf. Sci.* 464 (2019) 472–478.
- [19] B. Joshi, E. Samuel, M.-W. Kim, S. Park, M.T. Swihart, W.Y. Yoon, S.S. Yoon, Atomic-layer-deposited TiO₂-SnZnO/carbon nanofiber composite as a highly stable, flexible and freestanding anode material for lithium-ion batteries, *Chem. Eng. J.* 338 (2018) 72–81.
- [20] J. Park, J.-B. Ju, W. Choi, S.-O. Kim, Highly reversible ZnO@ZIF-8-derived nitrogen-doped carbon in the presence of fluoroethylene carbonate for high-performance lithium-ion battery anode, *J. Alloys Compd.* 773 (2019) 960–969.
- [21] Y. Zhang, K. Hu, J. Ren, Y. Wu, N. Yu, A. Feng, Z. Huang, Z. Jia, G. Wu, A sandwich-like Si/SiC/nanographite sheet as a high performance anode for lithium-ion batteries, *Dalton Trans.* 48 (2019) 17683–17690.
- [22] H. Yue, Z. Shi, Q. Wang, Z. Cao, H. Dong, Y. Qiao, Y. Yin, S. Yang, MOF-derived cobalt-doped ZnO@C composites as a high-performance anode material for lithium-ion batteries, *ACS Appl. Mater. Interfaces* 6 (2014) 17067–17074.
- [23] B.M. Basavaraja, S.B. Majumder, A. Sharma, Electrospun hollow glassy carbon–reduced graphene oxide nanofibers with encapsulated ZnO nanoparticles: a free standing anode for Li-ion batteries, *J. Mater. Chem.* 3 (2015) 5344–5351.
- [24] X. Sun, C. Zhou, M. Xie, H. Sun, T. Hu, F. Lu, S.M. Scott, S.M. George, J. Lian, Synthesis of ZnO quantum dot/graphene nanocomposites by atomic layer deposition with high lithium storage capacity, *J. Mater. Chem.* 2 (2014) 7319–7326.
- [25] M. Yu, D. Shao, F. Lu, X. Sun, H. Sun, T. Hu, G. Wang, S. Sawyer, H. Qiu, J. Lian, ZnO/graphene nanocomposite fabricated by high energy ball milling with greatly enhanced lithium storage capability, *Electrochem. Commun.* 34 (2013) 312–315.
- [26] N.P. Wagner, A. Tron, J.R. Tolchard, G. Noia, M.P. Bellmann, Silicon anodes for lithium-ion batteries produced from recovered kerf powders, *J. Power Sources* 414 (2019) 486–494.
- [27] Z. Wang, Z. Wang, L. Yang, H. Wang, Y. Song, L. Han, K. Yang, J. Hu, H. Chen, F. Pan, Boosting interfacial Li⁺ transport with a MOF-based ionic conductor for solid-state batteries, *Nano energy* 49 (2018) 580–587.
- [28] Z. Yang, J. Wang, H.-T. Wu, F.-J. Kong, W.-Y. Yin, H.-J. Cheng, X.-Y. Tang, B. Qian, S. Tao, J. Yi, MOFs derived Co_{1-x}S nanoparticles embedded in N-doped carbon nanosheets with improved electrochemical performance for lithium ion batteries, *Appl. Surf. Sci.* 479 (2019) 693–699.
- [29] Y. Han, P. Qi, S. Li, X. Feng, J. Zhou, H. Li, S. Su, X. Li, B. Wang, A novel anode material derived from organic-coated ZIF-8 nanocomposites with high performance in lithium ion batteries, *Chem. Commun.* 50 (2014) 8057–8060.
- [30] G. Zheng, M. Chen, H. Zhang, J. Zhang, X. Liang, M. Qi, J. Yin, Zn-MOFs derived porous carbon nanofiber for high performance lithium-ion batteries, *Surf. Coating. Technol.* 359 (2019) 384–389.
- [31] T. Mehtab, G. Yasin, M. Arif, M. Shakeel, R.M. Korai, M. Nadeem, N. Muhammad, X. Lu, Metal-organic frameworks for energy storage devices: batteries and supercapacitors, *J. Energy Storage* 21 (2019) 632–646.
- [32] A. Baniani, C. Chmelik, E.M. Forman, L. Fan, E. Zhou, F. Zhang, R. Lyndon, R.P. Lively, S. Vasenkov, Anomalous relationship between molecular size and diffusivity of ethane and ethylene inside crystals of zeolitic imidazolate framework-11, *J. Phys. Chem. C* 123 (2019) 16813–16822.
- [33] Y. Liu, B. Hu, S. Wu, M. Wang, Z. Zhang, B. Cui, L. He, M. Du, Hierarchical nanocomposite electrocatalyst of bimetallic zeolitic imidazolate framework and MoS₂ sheets for non-Pt methanol oxidation and water splitting, *Appl. Catal. B Environ.* 258 (2019) 117970.
- [34] M. Gomar, S. Yeganegi, Adsorption of 5-Fluorouracil and Thioguanine drugs into ZIF-1, ZIF-3 and ZIF-6 by simulation methods, *Mater. Sci. Eng. C* 97 (2019) 461–466.
- [35] Q. Gan, K. Zhao, S. Liu, Z. He, Solvent-free synthesis of N-doped carbon coated ZnO nanorods composite anode via a ZnO support-induced ZIF-8 in-situ growth strategy, *Electrochim. Acta* 250 (2017) 292–301.
- [36] Q. Li, H. Zhang, S. Lou, Y. Qu, P. Zuo, Y. Ma, X. Cheng, C. Du, Y. Gao, G. Yin, Pseudocapacitive Li⁺ intercalation in ZnO/ZnO@C composites enables high-rate lithium-ion storage and stable cyclability, *Ceram. Int.* 43 (2017) 11998–12004.
- [37] T. Kim, H. Kim, J.-M. Han, J. Kim, ZnO-embedded N-doped porous carbon nanocomposite as a superior anode material for lithium-ion batteries, *Electrochim. Acta* 253 (2017) 190–199.
- [38] S. An, B. Joshi, A.L. Yarin, M.T. Swihart, S.S. Yoon, Supersonic cold spraying for energy and environmental applications: one-step scalable coating Technology for advanced micro- and nanotextured materials, *Adv. Mater.* 32 (2020) 1905028.
- [39] J.-G. Lee, B.N. Joshi, J.-H. Lee, T.-G. Kim, D.-Y. Kim, S.S. Al-Deyab, I.W. Seong, M.T. Swihart, W.Y. Yoon, S.S. Yoon, Stable high-capacity lithium ion battery anodes produced by supersonic spray deposition of hematite nanoparticles and self-healing reduced graphene oxide, *Electrochim. Acta* 228 (2017) 604–610.
- [40] D.-Y. Kim, B.N. Joshi, J.-G. Lee, J.-H. Lee, J.S. Lee, Y.K. Hwang, J.-S. Chang, S. Al-Deyab, J.-C. Tan, S.S. Yoon, Supersonic cold spraying for zeolitic metal–organic framework films, *Chem. Eng. J.* 295 (2016) 49–56.
- [41] Q. Shi, Z. Chen, Z. Song, J. Li, J. Dong, Synthesis of ZIF-8 and ZIF-67 by steam-assisted conversion and an investigation of their tribological behaviors, *Angew. Chem. Int. Ed.* 50 (2011) 672–675.
- [42] Y.-R. Lee, M.-S. Jang, H.-Y. Cho, H.-J. Kwon, S. Kim, W.-S. Ahn, ZIF-8: a comparison of synthesis methods, *Chem. Eng. J.* 271 (2015) 276–280.
- [43] B. Chen, Z. Yang, Y. Zhu, Y. Xia, Zeolitic imidazolate framework materials: recent progress in synthesis and applications, *J. Mater. Chem.* 2 (2014) 16811–16831.
- [44] A.S. Munn, P.W. Dunne, S.V.Y. Tang, E.H. Lester, Large-scale continuous hydrothermal production and activation of ZIF-8, *Chem. Commun.* 51 (2015) 12811–12814.
- [45] L.S. Lai, Y.F. Yeong, N.C. Ani, K.K. Lau, A.M. Shariff, Effect of synthesis parameters on the formation of zeolitic imidazolate framework 8 (ZIF-8) nanoparticles for CO₂ Adsorption, *Part. Sci. Technol.* 32 (2014) 520–528.
- [46] D.-Y. Kim, S. Sinha-Ray, J.-J. Park, J.-G. Lee, Y.-H. Cha, S.-H. Bae, J.-H. Ahn, Y.C. Jung, S.M. Kim, A.L. Yarin, S.S. Yoon, Self-healing reduced graphene oxide films by supersonic kinetic spraying, *Adv. Funct. Mater.* 24 (2014) 4986–4995.
- [47] X. He, L. Bi, Y. Li, C. Xu, D. Lin, CoS₂ embedded graphitic structured N-doped carbon spheres interlinked by rGO as anode materials for high-performance sodium-ion batteries, *Electrochim. Acta* 332 (2020) 135453.
- [48] Z. Sun, C. Zhao, X. Cao, K. Zeng, Z. Ma, Y. Hu, J.-H. Tian, R. Yang, Insights into the phase transformation of NiCo₂S₄@rGO for sodium-ion battery electrode, *Electrochim. Acta* 338 (2020) 135900.
- [49] R. Li, W. Yue, X. Chen, Fabrication of porous carbon-coated ZnO nanoparticles on electrochemical exfoliated graphene as an anode material for lithium-ion batteries, *J. Alloys Compd.* 784 (2019) 800–806.
- [50] J. Cravillon, R. Nayuk, S. Springer, A. Feldhoff, K. Huber, M. Wiebcke, Controlling zeolitic imidazolate framework nano- and microcrystal formation: insight into crystal growth by time-resolved in situ static light scattering, *Chem. Mater.* 23 (2011) 2130–2141.
- [51] K. Kida, M. Okita, K. Fujita, S. Tanaka, Y. Miyake, Formation of high crystalline ZIF-8 in an aqueous solution, *CrystEngComm* 15 (2013) 1794.
- [52] H. Zhang, J. Huo, H. Yang, F. Li, C. Duan, H. Xi, Green and rapid preparation of hierarchically porous metal–organic zeolites and simulation of their growth, *J. Mater. Chem.* 7 (2019) 1022–1029.
- [53] H. Yin, J. Shang, J. Choi, A.C.K. Yip, Generation and extraction of hydrogen from low-temperature water–gas-shift reaction by a ZIF-8-based membrane reactor, *Microporous Mesoporous Mater.* 280 (2019) 347–356.
- [54] T. Zhou, Y. Sang, X. Wang, C. Wu, D. Zeng, C. Xie, Pore size dependent gas-sensing selectivity based on ZnO@ZIF nanorod arrays, *Sensor. Actuator. B Chem.* 258 (2018) 1099–1106.
- [55] R. Kant, S. Pathak, V. Dutta, Design and fabrication of sandwich-structured α -Fe₂O₃/Au/ZnO photoanode for photoelectrochemical water splitting, *Sol. Energy Mater. Sol. Cell.* 178 (2018) 38–45.
- [56] S. Soumya, V. Sheemol, P. Amba, A.P. Mohamed, S. Ananthakumar, Sn and Ag doped ZnO quantum dots with PMMA by in situ polymerization for UV/IR protective, photochromic multifunctional hybrid coatings, *Sol. Energy Mater. Sol. Cell.* 174 (2018) 554–565.
- [57] F. Bai, Y. Xia, B. Chen, H. Su, Y. Zhu, Preparation and carbon dioxide uptake capacity of N-doped porous carbon materials derived from direct carbonization of zeolitic imidazolate framework, *Carbon* 79 (2014) 213–226.
- [58] X. Zhou, Z. Jia, A. Feng, X. Wang, J. Liu, M. Zhang, H. Cao, G. Wu, Synthesis of fish skin-derived 3D carbon foams with broadened bandwidth and excellent electromagnetic wave absorption performance, *Carbon* 152 (2019) 827–836.
- [59] X. Chen, T. Shi, K. Zhong, G. Wu, Y. Lu, Capacitive behavior of MoS₂ decorated with FeS₂@carbon nanospheres, *Chem. Eng. J.* 379 (2020) 122240.
- [60] B. Liu, X. Hu, H. Xu, W. Luo, Y. Sun, Y. Huang, Encapsulation of MnO nanocrystals in electrospun carbon nanofibers as high-performance anode materials for lithium-ion batteries, *Sci. Rep.* 4 (2014) 4229.
- [61] E. Samuel, H.S. Jo, B. Joshi, S. An, H.G. Park, Y.I. Kim, W.Y. Yoon, S.S. Yoon, Decoration of MnO nanocrystals on flexible freestanding carbon nanofibers for lithium ion battery anodes, *Electrochim. Acta* 231 (2017) 582–589.
- [62] Y.J. Mai, D. Zhang, Y.Q. Qiao, C.D. Gu, X.L. Wang, J.P. Tu, MnO/reduced graphene oxide sheet hybrid as an anode for Li-ion batteries with enhanced lithium storage performance, *J. Power Sources* 216 (2012) 201–207.
- [63] J. Moulder, W. Stickle, P. Sobol, K. Bomben, in: J. Chastain (Ed.), *Handbook of X-Ray Photoelectron Spectroscopy*, 1992, p. 118. Perkin-Elmer, Eden Prairie, MN, 1992.
- [64] P. Ilanchezhian, G.M. Kumar, F. Xiao, A. Madhankumar, C. Siva, S.U. Yuldashev, H. Cho, T. Kang, Interfacial charge transfer in ZnTe/ZnO nano arrayed heterostructures and their improved photoelectronic properties, *Sol. Energy Mater. Sol. Cell.* 183 (2018) 73–81.